Phonon-glass dynamics in thermoelectric clathrates

Yaping Liu,[1] Qing Xi,[1] Jun Zhou,[1,*] Tsuneyoshi Nakayama,[1,2,†] and Baowen Li[3,‡]
[1]*Center for Phononics and Thermal Energy Science, School of Physics Science and Engineering, Tongji University, 200092 Shanghai, People's Republic of China*
[2]*Hokkaido University, Sapporo 060-0826, Japan*
[3]*Department of Mechanical Engineering, University of Colorado, Boulder, Colorado 80309, USA*
(Received 7 December 2015; revised manuscript received 26 April 2016; published 9 June 2016)

Type-I clathrate compounds exhibit glasslike thermal/dynamic properties due to symmetry breaking of guest-atom positions in tetrakaidecahedron cages. All of these features are associated with the phonon dynamics in the THz region, for which we perform large-scale numerical simulations by highlighting the difference between type-I clathrates $Ba_8Ga_{16}Ge_{30}$ (BGG) with on-center guest atoms and $Ba_8Ga_{16}Sn_{30}$ (BGS) with off-center guest atoms. The results of the phonon densities of states $D(\omega)$, the dynamic structure factors $S(\boldsymbol{Q},E)$, the specific heats $C(T)$, and the participation ratios of eigenmodes clearly realize a drastic change from the conventional phonon dynamics of BGG to the phonon-glass dynamics of BGS.

DOI: 10.1103/PhysRevB.93.214305

I. INTRODUCTION

Clathrate compounds represent a physical realization of the phonon-glass electron-crystal concept [1,2], one of the guiding principles for exploring high-performance thermoelectric materials. Type-I clathrates are particularly interesting in this respect since off-center systems (OFS) exhibit glasslike thermal/dynamic behaviors different from those of on-center systems (ONS). In OFS, the specific heat $C(T)/T^3$ exhibits a broad peak at a few Kelvins identical to the boson peak observed in structural glasses, in addition to glasslike phonon thermal conductivities [3]. It is remarkable that although these compounds possess a crystalline cubic structure on host cages, they show glasslike thermal/dynamic properties [4]. All of these features are associated with the THz-frequency phonon dynamics in type-I clathrate compounds. There has been no quantitative theoretical investigation of the mechanism underlying the glasslike thermal/dynamics properties, so this subject remains as an open and challenging problem.

Type-I clathrates are formed from networked cages consisting of large tetrakaidecahedrons (14-hedrons) and small dodecahedrons (12-hedrons), in which the group-I or -II elements in the periodic table are encaged as guest atoms. The guest atoms in the dodecahedron and tetrakaidecahedron are denoted by (1) and (2) sites, respectively (see Fig. 1). Phonon dynamics of type-I clathrates with on-center guest atom (2) has been recently investigated in terms of first-principles calculations for a unit cell containing 54 atoms [5–7]. The ONS possess the symmetry of translational invariance, which makes it possible to reduce the system size by employing the periodic boundary conditions when performing computer simulations. However, type-I clathrates with off-center guest atom (2) lack translational invariance, as evident from experimental observations of their glasslike behaviors [3]. In order to overcome this system-size problem, the performance of large-scale numerical simulations is needed.

This paper aims to theoretically reveal the microscopic mechanism underlying phonon-glass dynamics at THz frequencies (<10 meV) in type-I clathrates by highlighting the difference between ONS and OFS. We perform large-scale numerical simulations by treating $10^7 \times 10^7$ sizes of matrices on the THz-frequency phonon dynamics of OFS by illustrating type-I $Ba_8Ga_{16}Sn_{30}$ (BGS) as prototype materials as well as on-center $Ba_8Ga_{16}Ge_{30}$ (BGG) belonging to ONS for comparison. All of the crystalline and glasslike features are realized in these materials; in addition, spectroscopic data in the THz-frequency region is fully available. See Table 1 in Ref. [3] for the detailed classification of ONS or OFS for various type-I clathrates.

II. SCOPE AND METHODS

We employ an efficient computational algorithm called the forced oscillator method (FOM) [8,9]. The FOM is suitable for our purpose as described in the Supplemental Material [10]. We focus our attention on the phonon dynamics in the THz-frequency region and below, since the dynamics at these frequencies manifests remarkable differences between ONS and OFS. Phonon modes higher than a few THz related to the deformation of cages and the vibrations of guest atom (1) in the smaller cage of dodecahedron are beyond the scope of our study. This enables us to describe the THz-frequency phonon dynamics under a coarse-grained Hamiltonian, as proposed in Sec. III. At first, we construct coarse-grained Hamiltonians in order to focus our attention on the phonon dynamics in the THz-frequency region and below, namely, acoustic modes and low-lying optical modes. Next, we give the numerical results of the spectral density of states $D(\omega)$, the dynamic structure factors $S(\boldsymbol{Q},E)$, and the specific heats $C(T)/T^3$. These results clearly provide a drastic change from the conventional phonon dynamics of ONS to the glasslike dynamics of OFS. On this basis, we give the microscopic origin underlying glasslike thermal/dynamics behaviors in type-I clathrates with off-center guest atoms.

*zhoujunzhou@tongji.edu.cn
†tnaka@eng.hokudai.ac.jp
‡baowen.li@colorado.edu

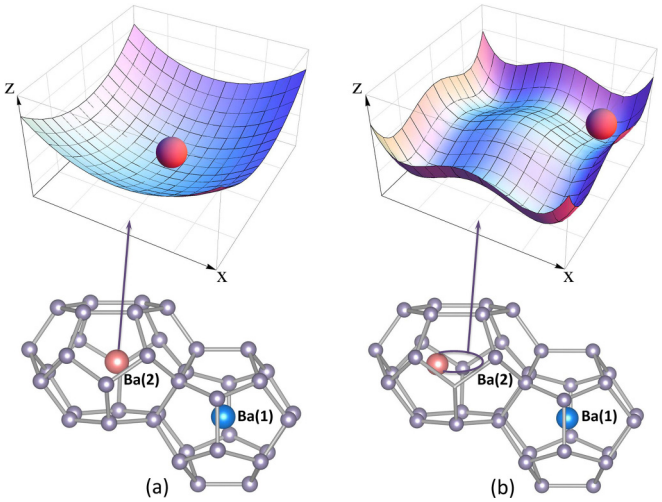

FIG. 1. The lower molecular units give a tetrakaidecahedral cage with guest atom Ba(2) at (a) the 6*d* site in on-center BGG and (b) the 24*k* site in off-center BGS, and smaller dodecahedral cage encapsulating Ba(1) at the 2*a* site. The upper (a) and (b) are the schematic illustrations of the wine-glass potential for $\xi > 0, \eta > 0$ in Eq. (1) and wine-bottle type potential for $\xi < 0, \eta > 0$ in Eq. (1).

III. COARSE-GRAINED HAMILTONIAN FOR ONS AND OFS

The length scale λ of phonons at the frequency region of $\nu \leqslant 2 \sim 3$ THz ($E \leqslant 8 \sim 12$ meV) becomes $\lambda \geqslant 1$ nm, which is larger than the size of a unit cell of $a \simeq 1$ nm in type-I clathrates, as estimated from the relation $\lambda = v/\nu$ using the sound velocity v. This indicates the invalidity of describing THz-frequency dynamics from a single unit cell of $a \simeq 1$ nm, especially for the case of OFS. For this situation, it is reasonable to adopt the coarse-grained Hamiltonian rather than treating all microscopic constituents of 54 atoms in a unit cell as equally relevant degrees of freedom. In line with the coarse-grained scenario, we describe the guest atom Ba(2) as having mass m and the tetrakaidecahedron and dodecahedron cages with the total mass M excluding the guest atom (2). See the molecular unit in Fig. 1. The position vector of the ℓth cage at time t is defined as $\boldsymbol{R}_\ell + \boldsymbol{r}_\ell(t)$, where $\boldsymbol{R}_\ell$ is the equilibrium position of the ℓth cage center, and $\boldsymbol{r}_\ell(t)$ represents a small deviation from $\boldsymbol{R}_\ell$. The position of guest atom Ba(2) is given by the vector $\boldsymbol{U}_\ell + \boldsymbol{u}_\ell(t)$ measured from the cage center, where $\boldsymbol{u}_\ell(t)$ is a small deviation from the randomly oriented position $\boldsymbol{U}_\ell$ of Ba(2). It is apparent that $\boldsymbol{U}_\ell = 0$ is the case of on-center guest atom in ONS, whereas the off-center case corresponds to $\boldsymbol{U}_\ell \neq 0$ in OFS. The actual deviation is $|\boldsymbol{U}_0| = 0.43$ Å for type-I BGS [11].

The shape of the tetrakaidecahedron distinguishes the vibrations of guest atoms in the plane parallel and perpendicular to the hexagonal face of the cage (x-y plane in Fig. 1). The guest atoms Ba(2) in BGG and BGS execute in-plane vibration parallel to the x-y plane in addition to out-of-plane motions along the z axis [12]. In order to describe in a unified way both the vibrations of on-center and off-center guest atoms (2), we consider the potentials such as those depicted in Figs. 1(a) and 1(b).

By keeping up to the fourth order of small "relative" displacement $|\boldsymbol{u}_\ell(t) - \boldsymbol{r}_\ell(t)|$, the potential function between the guest atom (2) and the cage is described by

$$V_4 = \sum_{\ell,\alpha=x,y} \frac{1}{2}\Big[\xi |U_{\ell,\alpha} + u_{\ell,\alpha}(t) - r_{\ell,\alpha}(t)|^2 + \frac{\eta}{2}|U_{\ell,\alpha} + u_{\ell,\alpha}(t) - r_{\ell,\alpha}(t)|^4\Big]. \quad (1)$$

This modified Higgs-type potential involves two different types of potentials depending on a plus or minus sign of ξ: the case of $\xi, \eta > 0$ yields the wine-glass-type potential of Fig. 1(a) with $\boldsymbol{U}_\ell = 0$, and the case of $\xi < 0, \eta > 0$ gives rise to the wine-bottle-type potential of Fig. 1(b) with $\boldsymbol{U}_\ell \neq 0$. Thus, Eq. (1) enables us to treat the vibrational motions of Ba(2) for both ONS and OFS in a unified manner. Imposing the condition $\xi < 0, \eta > 0$ in Eq. (1), we have the potential with the minimum at $V_{4,\min} = -\xi^2/4\eta$ at $|\boldsymbol{U}_\ell|^2 = -\xi/\eta$. The nonzero vector $\boldsymbol{U}_\ell$ presents the local rotation symmetry breaking of off-center guest atoms in tetrakaidecahedron as seen in the following.

The anharmonicity of the potential becomes irrelevant at temperatures lower than several tens Kelvin as evident from the temperature dependences of optical spectroscopies and thermal conductivities for ONS and OFS [3]. So, the harmonic model is good enough in order to reveal the details underlying phonon-glass dynamics in type-I clathrates at the THz-frequency region. We can expand Eq. (1) in terms of the small relative displacement $|\boldsymbol{u}_\ell(t) - \boldsymbol{r}_\ell(t)|$ of Ba(2) around the equilibrium position $\boldsymbol{U}_0$ by keeping up to the harmonic terms around the equilibrium position.

For Ba(2) in ONS, the coupling potential between cage and on-center guest atom (2) deduced from Eq. (1) is expressed by

$$V_{\rm CG}^{\rm ON} = \sum_{\ell,\lambda=\rm in,out} \frac{\xi_\lambda}{2}[\boldsymbol{u}_{\ell,\lambda}(t) - \boldsymbol{r}_{\ell,\lambda}(t)]^2, \quad (2)$$

where ξ_λ represents the force constants between the cage and the guest atom. The force constant $\xi_{\rm in}$ relates to the in-plane motion around $|\boldsymbol{U}_\ell| = 0$ parallel to the x-y plane, and the force constant $\xi_{\rm out}$ relates to the out-of-plane motion.

For Ba(2) in OFS, we express the position of off-center Ba(2) at time t in the x-y plane by $[U_0 + \delta r_\ell(t)]e^{i[\theta_\ell + \delta\theta_\ell(t)]}$. The phase factor $\delta\theta_\ell(t)$ describes libration motion around the randomly oriented angle θ_ℓ at the ℓth site due to local rotation symmetry breaking. Note that both $\delta\theta_\ell(t)$ and $\delta r_\ell(t)$ are dynamical variables of Ba(2) given by the relative coordinate. The potential function can be expanded around U_0 and θ_ℓ in terms of small deviation $\delta r_\ell(t)$ and $\delta\theta_\ell(t)$, for which we introduce the force constants ξ_s and ξ_θ for stretching and angular motion, in addition to the one ξ_ϕ for out-of-plane vibration. Thus, the potential between off-center guest (2) and cage can be expressed as

$$V_{\rm CG}^{\rm OF} = \frac{1}{2}\sum_\ell \left(\xi_s \delta r_\ell^2 + \xi_\theta U_0^2 \delta\theta_\ell^2 + \xi_\phi U_0^2 \delta\phi_\ell^2\right). \quad (3)$$

The force constants ξ_s and ξ_θ represent the coupling between vibrations of the guest atoms (2) and acoustic phonons coming from network cages, which we describe in detail in the part

showing the calculated results of $D(\omega)$ and $S(\boldsymbol{Q},E)$ for off-center BGS in Sec. V.

Our coarse-grained system consisting of combined cages of tetrakaidecahedron and dodecahedron with mass M forms a primitive cubic structure ($Pm\bar{3}n$). Each cage is elastically connected with nearest-neighbor cages by the force constants $f_\parallel, f_\perp$, which represent longitudinal ($\parallel$) and transverse ($\perp$) acoustic modes propagating along host cages. Using these quantities, the potential energy concerning the cage-cage interaction is expressed as

$$V_{CC} = \sum_{\ell>\ell',\mu} \frac{f_{\ell,\ell',\mu}}{2}[\boldsymbol{r}_\ell(t) - \boldsymbol{r}_{\ell'}(t)]^2, \tag{4}$$

where $\mu = \parallel, \perp, \perp'$. We keep only the nearest-neighbor coupling $\ell' = \ell - 1$ between cages denoted by $f_\parallel$, $f_\perp$, and $f_{\perp'}$. The kinetic energy is expressed by $K = \frac{1}{2}\sum_\ell (M\dot{\boldsymbol{r}}_\ell^2 + m\ddot{\boldsymbol{u}}_\ell^2)$. The total Hamiltonian H is expressed by the sum of these relations, $H = K + V_{CC} + V_{CG}^{\mathrm{ON(OF)}}$.

IV. RESULTS OF $D(\omega)$ and $S(\boldsymbol{Q},E)$ FOR ON-CENTER BGG

The force constants $f_\parallel, f_\perp (= f_{\perp'})$ of on-center BGG in Eq. (4) can be determined from the sound velocities $v_\parallel = 4096$ m/s and $v_\perp = 2700$ m/s obtained from coherent inelastic neutron scattering (INS) [14,15]. These give rise to $f_\parallel = 17.5$ and $f_\perp = 7.59$ N/m from the relation $v_\mu = a[f_\mu/(m+M)]^{1/2}$ taking $M = 4.32m$ and the lattice constant $a = 10.78$ Å.

Mori *et al.* [16] have assigned the peaks at $\nu = 1.15$ THz ($= 4.76$ meV) as the in-plane vibration of Ba(2) in the x-y plane and $\nu = 1.80$ THz (7.44 meV) as the out-of-plane motion. These assignments accord with those of Raman scattering experiments for BGG [17], where the lower peaks at $\nu = 0.96$ and $\nu = 1.81$ THz have been observed. From the above assignments for BGG [16], the force constant ξ_{in} for BGG is evaluated as $\xi_{\mathrm{in}} = 9.64$ N/m from the relation $\omega_0^2 = \xi_{\mathrm{in}}(1 + m/M)/m$, while the force constant ξ_{out} becomes $\xi_{\mathrm{out}} = 23.62$ N/m.

Figure 2 gives the results of $D(\omega)$ and $S(\boldsymbol{Q},E)$ along $\boldsymbol{Q} = (222)+[\mathrm{h}00]$, $\boldsymbol{Q} = (033)+[\mathrm{h}00]$, and $\boldsymbol{Q} = (400)+[\mathrm{h}00]$ for BGG. The actual form of $S(\boldsymbol{Q},E)$ with the definition of the scattering vector $\boldsymbol{Q}$ is given in the Supplemental Material [13]. Figure 2(a) shows three peaks in $D(\omega)$: the first sharp peak at 4.0 meV (0.97 THz), the next rather broad peak at 5.2 meV (1.25 THz), and the third one at 7.9 meV (1.91 THz). There exists a quasigap at around 4.5 meV in $D(\omega)$, as seen from Fig. 2(a). The first peak in $D(\omega)$ in Fig. 2(a) is attributed to the flat end of the longitudinal acoustic (LA) branch and the second one is attributed to the flat part of the optic mode close to the Γ point, as seen from Figs. 2(b)–2(d). The third peak at 7.9 meV is due to the out-of-plane vibrations of Ba(2) perpendicular to the x-y plane as found in Fig. 2(c). As seen from Fig. 2(c), our calculated results show good agreement with the INS data [14], validating our model Hamiltonian.

The calculated intensities of $S(\boldsymbol{Q},E)$ marked by color scale in Figs. 2(b)–2(d) come from the scalar product of the eigenvector $\boldsymbol{e}_m(\lambda)$ of the excited mode and the scattering vector $\boldsymbol{Q}$ given in Eq. (14) in the Supplemental Material [13]. Our model reproduces these intensities of $S(\boldsymbol{Q},E)$ observed by INS experiments. We emphasize that caution is needed to interpret the data plotted by FWHM [14] or Gaussian fits [15], in particular for the case in which the spectra are close together such as those of type-I clathrates with a unit cell containing 54 atoms.

Our calculations have been performed using the minimum number (four) of force constants: $f_\parallel, f_\perp, \xi_{\mathrm{in}}, \xi_{\mathrm{out}}$. It should be emphasized that we have not adopted the spectroscopic data at the end of the Brillouin zone to determine these force constants. The density of states (DOS) for on-center BGG shown in Fig. 2(a) indicates that the first sharp peak appears at 4.0 meV, while the DOS for BGG obtained from *ab initio* calculation [7] indicates that the first sharp peak appears at 28 cm^{-1} = 3.5 meV, which is smaller than our result.

We should mention that the INS experiments for a powder sample of BGG yield the first peak at 4.0 meV at 100 K [18]. The integrated intensity of $S(\boldsymbol{Q},E)$ over upper half Brillouin zone along (004) + [hh0] for a single crystal obtained from coherent INS by Nakamura and Arai [19] provides the first sharp peak at 4.0 meV at 5 K, as seen in Fig. 38 in Ref. [3]. Note that this peak arises from the flat end of the dispersion curves of acoustic phonons, *not* from the spectra of optic modes at the Γ point. The agreement with our calculations at 4.0 meV is *remarkable*, though the spectroscopic data at the end of the Brillouin zone are not adopted in determining the four force constants. These results surely validate our coarse-grained model Hamiltonian.

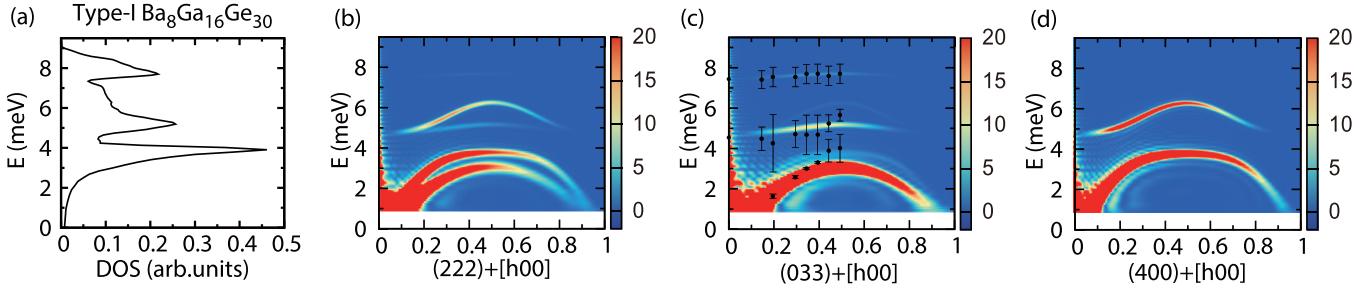

FIG. 2. The results of $D(\omega)$ of (a) type-I BGG and (b)–(d) $S(\boldsymbol{Q},E)E/q^2[n(E)+1]$ for various scattering vectors $\boldsymbol{Q} = \boldsymbol{G}+[\mathrm{h}00]$. The color scale indicates the intensity as a function of the energy transfer E_q. Panels (b-d) employ the same Brillouin zone as that of Ref. [14]. Panel (b) include both transverse and longitudinal acoustic modes coupled with in-plane motion ξ_{in} and with out-of-plane motion ξ_{out}, while (c) and (d) present transverse and longitudinal acoustic modes, respectively, as a result of the selection rules on $S(\boldsymbol{Q},E)$ given in Table 1 in the Supplemental Material [13]. The black dots in (c) with error bars of the FWHM are INS data [14]. The calculations were performed for $100 \times 100 \times 100$ unit cells.

The low-lying optic modes attributed to the vibrations of guest atom Ba(2) are hybridized with acoustic modes above the middle of the first Brillouin zone. This hybridization arises from the anticrossing between acoustic modes due to host cages and optical modes concerning Ba(2). A detailed description of hybridization and selection rules for $S(\boldsymbol{Q},E)$ is provided in Table 1 in the Supplemental Material [13].

The anharmonic effects should be realized as the blue shift of the lowest optical spectra relevant to the guest atom Ba(2) [18,19], which we do not address in this paper since the essential mechanism of THz-frequency phonon dynamics is involved in the harmonic treatment [20–22]. It should be emphasized that our model employing the smallest number of force constants has the advantage, compared to the model with a much greater number of force constants, to clarify the microscopic origin underlying the glasslike dynamic behaviors in OFS in the THz-frequency region, as seen in the next section.

V. $D(\omega)$ and $S(\boldsymbol{Q},E)$ OF OFF-CENTER BGS

Here we consider the effect of the random orientation of off-center guest ions $Ba^{++}(2)$ on the emergence of glasslike phonon dynamics in off-center BGS. Figure 1(b) depicts the potential well of $24k$ sites in a tetrakaidecahedron cage obtained by assuming the short-range interaction between Ba^{++} and cage ions. However, the guests Ba^{++} yield the long-range Coulomb interaction between surrounding ions, which causes the random orientation of guest ions due to dipole-dipole interactions, as described in detail in Ref. [3]. We should note that the dipole-dipole interactions lower the total potential energy of the system. The effect of the randomly oriented dipole $(2e)^*\boldsymbol{U}_\ell$ at the ℓth site should be taken into account in the coupling between the vibrations of Ba(2) and acoustic modes arising from the cage network via ξ_s and ξ_θ in Eq. (3). Note here that the p- and n-type dependence of the observed thermal/dynamic behaviors on BGG and BGS comes from the difference of the shielding effect to electric dipoles.

To understand this configuration-dependent coupling, let us exemplify the case in which transverse acoustic (TA) phonons are incident along the z axis in Fig. 1(b). For off-center Ba(2) taking the right-side position on the x axis, TA phonons with the polarization parallel to the x axis couple with the stretching component $\delta r_\ell(t)$ with the force constant ξ_s. If the off-center Ba(2) guest atom takes on the position along the y axis, the above TA phonon couples with the libration component $U_0\delta\theta_\ell(t)$ via the force constant ξ_θ. Provided that Ba(2) takes a position $(U_0\cos\theta_\ell, U_0\sin\theta_\ell)$ on the x-y plane in Fig. 1(b), the TA modes with the polarization parallel to the x axis couple with libration and stretching vibrations at the same time via the force constants $\xi_{\ell,\theta}=\xi_\theta|\sin\theta_\ell|$ and $\xi_{\ell,s}=\xi_s|\cos\theta_\ell|$. Thus, the coupling constants depend on the randomly distributed angle θ_ℓ. The same argument holds for the coupling of longitudinal acoustic (LA) phonons with arbitrary polarization direction.

Actual values of the force constants ξ_θ and ξ_s for off-center BGS are obtained in the same manner as the case of on-center BGG. Mori *et al.* [23] observed by means of THz time-domain spectroscopy that the lowest-lying peak of BGS at 0.71 THz splits into double peaks: 0.5 THz (2.07 meV) and 0.72 THz (2.97 meV). This spectra should be assigned to the libration and stretching modes of Ba(2) associated with ξ_θ and ξ_s. The peak around 1.35 THz (5.58 meV) is assigned as the out-of-plane motion of Ba(2) to the hexagonal faces of the tetrakaidecahedron. Using these data, we can obtain the force constants as $\xi_\phi=14.03$, $\xi_\theta=1.93$, and $\xi_s=3.99$ N/m. The force constants $f_\parallel$ and $f_\perp(=f_{\perp'})$ in Eq. (4) for BGS are obtained using the sound velocities $v_\parallel=3369$ and $v_\perp=1936$ m/s [12] from the relation $v_\mu=a[f_\mu/(m+M)]^{1/2}$. These provide $f_\parallel=13.3$ and $f_\perp=4.38$ N/m by employing masses $m=137$ u for Ba(2) atom and $M=6.01m$ for the cage, and the lattice spacing $a=11.68$ Å.

The results for $D(\omega)$ and $S(\boldsymbol{Q},E)$ for off-center BGS are shown in Fig. 3. In Fig. 3(a), two sharp peaks appear in $D(\omega)$ at 2.7 meV (0.65 THz) and 5.8 meV (1.4 THz), in addition to the broad band at 3.0–3.6 meV (0.73–0.87 THz). In contrast with $D(\omega)$ for on-center BGG in Fig. 2(a), there exists no clear gap between 2.7 and 4.5 meV. We should note that the spectra of $S(\boldsymbol{Q},E)$ near the origins in Figs. 3(b)–3(d) are broadened, reflecting the weak violation of translational invariance as well as the parts between 2.7 and 4.5 meV. In addition, the strengths of spectra at the end of the Brillouin zone are weakened. These are in contrast with the case of BGG shown in Figs. 2(b)–2(d). This type of weak violation of translational invariance in $S(\boldsymbol{Q},E)$ has also been observed in silica glass by means of coherent INS by Inamura *et al.* [24]. The quasiperiodicity in the Brillouin zone [24] arises from the scaffold network in silica glass.

We can identify the modes relevant to these two peaks at 2.7 and 4.5 meV from the direct calculations of eigenmodes as follows: the lower broad peak is attributed to the hybridized

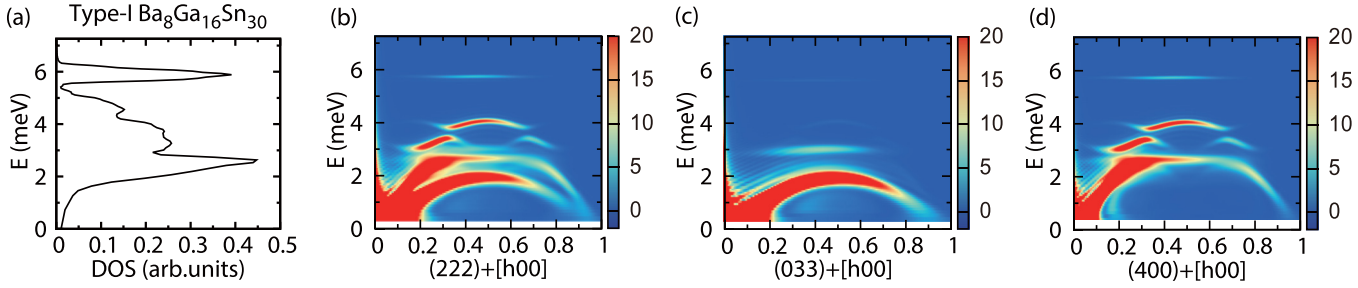

FIG. 3. The results of $D(\omega)$ of (a) type-I BGS and (b)–(d) $S(\boldsymbol{Q},E)E/q^2[n(E)+1]$ for various scattering vectors $\boldsymbol{Q}=\boldsymbol{G}+$[h00]. The color scale is the same as that defined in Fig. 2. Panels (b-d) employ the same Brillouin zone as that of Ref. [14]. The selection rules for $S(\boldsymbol{Q},E)$ on transverse and longitudinal modes are the same as the cases (b)–(d) given in the caption of Fig. 2. The calculations were performed for $99\times99\times99$ unit cells.

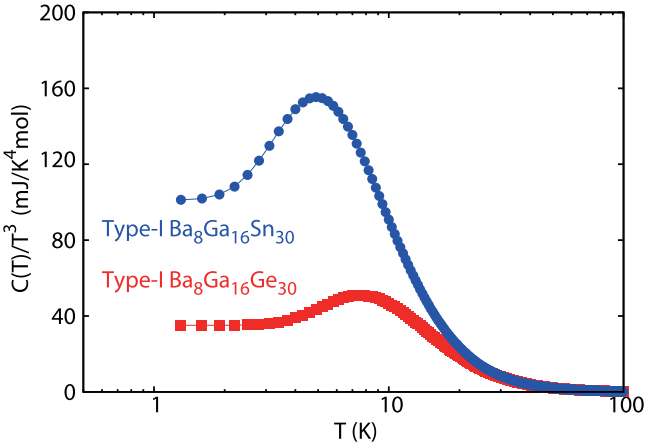

FIG. 4. Specific heats $C(T)/T^3$ vs T for on-center BGG (red squares) and off-center BGS (blue dots). The contribution from T-linear specific heats below 1 K due to two-level tunneling states in BGS is omitted [26].

modes between longitudinal/transverse acoustic modes and randomly oriented off-center Ba(2). In particular, the lowest peak at 3.0 meV is attributed to the hybridized modes between the longitudinal acoustic modes and libration motion of randomly oriented Ba(2).

The calculated results of $S(\boldsymbol{Q},E)$ for on-center BGG and off-center BGS for other scattering vectors $\boldsymbol{Q} = \boldsymbol{G}+$[hh0] are given in Figs. 3(a)–3(f) in the Supplemental Material [13]. These results clearly demonstrate the characteristic differences between on-center and off-center type-I clathrates.

VI. SPECIFIC HEATS OF BGG AND BGS

The calculated results for $C(T)/T^3$ depicted in Fig. 4 represent the broad hump at 5 K for BGS and the small hump at 10 K for BGG. The small hump in $C(T)/T^3$ of BGG results from the van Hove singularity in $D(\omega)$ at 4.0 meV in Fig. 2(a). The $C(T)/T^3$ for BGS reproduces well the boson peak observed in Ref. [12]. The hump at 4 K in BGS is attributed to the hybridized modes between low-lying optical modes associated with randomly oriented Ba(2) and TA/LA modes. Thus, the underlying mechanism of the broad hump of BGS is different from the hump at 10 K of BGG.

We have made clear that the heat capacities $C(T)/T^3$ in Fig. 4 are sensitive to the flat part at the end of dispersion curves of acoustic phonons. The first sharp peak in $D(\omega)$ for BGS originates from this flat dispersion curve and generates a broad hump in $C(T)/T^3$ at 5 K, as found in Fig. 4 (blue plots). This type of broad peak, the so-called boson peak, has been generally observed for various kinds of glassy systems [25]. However, caution is needed in asserting that the broad peak is a key signature of glassy behavior, for the following reasons. The expression of the specific heat $C(T)$ is given by

$$C(T) = -\frac{1}{k_B T^2}\frac{\partial}{\partial\beta}\left[\int_0^\infty n(\beta\hbar\omega)\hbar\omega D(\omega)d\omega\right], \qquad (5)$$

where $\beta = 1/k_B T$ and $n(\beta\hbar\omega)$ represents the Bose-Einstein distribution function, and $D(\omega)$ is the phonon density of states. When plotting the calculated $C(T)$ divided by T^3 from Eq. (5) in order to eliminate the contribution from the Debye phonons, the detailed information of glasslike phonon dynamics is averaged out by the integration in Eq. (5). It means that the broad peak at around several K should appear even in ordered systems if the van Hove singularity exists at around a few meV. Thus, it is inappropriate to assert "glasslike" only from the broad hump in the plot of $C(T)/T^3$. We need to identify the real nature of the relevant modes around a few meV underlying the glasslike phonon dynamics, as demonstrated in the next section.

VII. LOCALIZATION NATURES OF EIGENMODES

Here we study the localization natures of eigenmodes at the THz-frequency region for BGG and BGS in terms of large-scale numerical simulations. The localization natures of eigenmodes are sensitive to system size and boundary condition when performing computer simulations. For a sufficiently large system, there should be no difficulty in distinguishing between a localized mode and an extended mode. Our calculations have been performed for systems of $20 \times 20 \times 20$ unit cells employing a periodic boundary condition as all sites can be regarded as equally far from the boundary.

To characterize the localization nature of a relevant mode $\{\boldsymbol{e}_\ell(\varepsilon_q),\ \ell = 1,2,\ldots,N\}$ belonging to the eigenenergy ε_q, we calculate the participation ratio (PR) defined by

$$P(\varepsilon_q) = \frac{\left[\sum_{\ell=1}^N |\boldsymbol{e}_\ell(\varepsilon_q)|^2\right]^2}{N\sum_{\ell=1}^N |\boldsymbol{e}_\ell(\varepsilon_q)|^4}, \qquad (6)$$

where N is the total number of the cages and guest atoms. For extended states in an infinite system, $P(\varepsilon_q)$ approaches unity; however, $P(\varepsilon_q)$ takes values close to $\approx$0.5 for a system under periodic boundary condition, while $P(\varepsilon_q)$ becomes $1/N$ for strongly localized states. Therefore, the PR can be taken as a criterion to distinguish extended states from localized ones.

Figure 5(a) shows the PR of eigenmodes for on-center BGG as a function of ε_q. $P(\varepsilon_q)$ takes values around 0.4 between

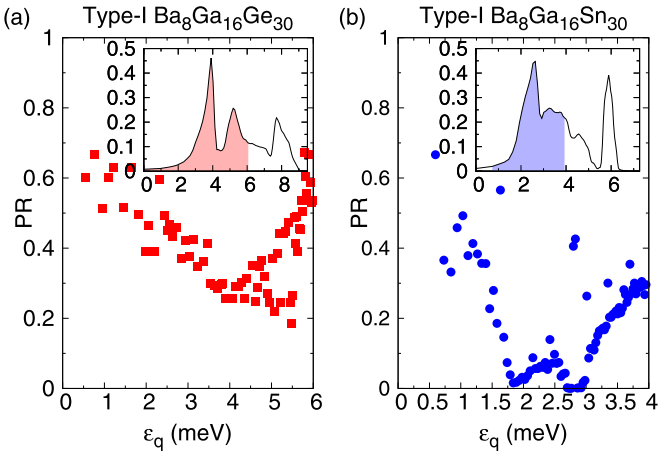

FIG. 5. The results of the participation ratio $P(\varepsilon_q)$ defined in Eq. (6) as a function of eigenenergy ε_q for (a) on-center BGG and (b) off-center BGS. The forced oscillator method (FOM) provides almost perfect convergence for DOS and PR with the system size $N = L \times L \times L$ from $L = 20$ to $L = 100$, as shown in Figs. 1 and 2 in Ref. [10]. The insets in (a) and (b) are the DOS marking calculated energy ranges.

0.5–6.2 meV indicating extended states. Figure 5(b) depicts the results of $P(\varepsilon_q)$ for off-center BGS. We should note that $P(\varepsilon_q)$ ranges from a value of strongly localized states $P(\varepsilon_q) \approx 0$ to extended states of $P(\varepsilon_q) \approx 0.5$. The clear distinction of $P(\varepsilon_q)$ at $\varepsilon_q = 1.5$ meV indicates that eigenmodes convert from extended to localized states *within* the acoustic band, which accords with the onset temperature of the plateau of BGS at 1.5 meV/$3.84k_B \approx 4.5$ K from the Wien's displacement law. The onset temperature is correlated with the strength of the force constant ξ_θ due to the hybridization with acoustic modes. The plateau indicates that the contribution of extended phonons saturates at $\kappa \approx 0.7$ W/Km for BGS. Thus, the onset of the plateau is apparently due to the localization of acoustic modes. The above result on BGS differs from the case of on-center BGG in Fig. 5(a), showing extended modes resulting from the symmetry of translational invariance.

VIII. SUMMARY AND CONCLUSIONS

We have performed large-scale simulations on the THz-frequency phonon dynamics in on-center BGG and off-center BGS by constructing the coarse-grained Hamiltonian given in Eqs. (1)–(4). This coarse-grained picture, rather than treating all microscopic constituents of 54 atoms in a unit cell as equally relevant degrees of freedom, has the advantage of revealing the microscopic origin on the emergence of glasslike dynamics at THz frequencies. The calculated results of $D(\omega)$, $S(\boldsymbol{Q},E)$, $C(T)/T^3$, and $P(\varepsilon_q)$ clearly manifest a drastic change from conventional phonon dynamics of BGG to phonon-glass dynamics of BGS, as shown in Figs. 2–5.

The agreement on the first sharp peak in the DOS at 4.0 eV between the INS data [18,19] and our results in Fig. 2(a) for BGG is remarkable. This first peak arises from the flat end of the dispersion curves of acoustic phonons, *not* from the spectra of optic modes at the Γ point. It should be emphasized that the spectroscopic data at the end of the Brillouin zone are not adopted in determining four force constants: $f_\parallel, f_\perp, \xi_{\rm in}, \xi_{\rm out}$. These results surely validate our coarse-grained model Hamiltonian, while the results of $D(\omega)$ and $S(\boldsymbol{Q},E)$ for BGS given in Fig. 3 show a broad band in the 2.7–4.0 meV range, in contrast to the cases of BGG given in Fig. 2. The broad band originates from the configuration-dependent coupling between vibrations of guest atoms (2) and acoustic modes from the host cage lattice.

In addition, we have demonstrated for off-center BGS that the acoustic phonons carrying heat convert to localized modes at 1.5 meV. Since this energy corresponds to the temperature 1.5 meV/$3.84k_B \approx 4.5$ K, this conversion should associate with the onset of the plateau thermal conductivities observed in off-center BGS [12]. In contrast, the THz-frequency phonon dynamics of on-center BGG behave in a conventional manner, reflecting the symmetry of translational invariance. In conclusion, our large-scale simulations have revealed the underlying mechanism of the glasslike phonon dynamics that emerges in off-center BGS. We conclude that randomly oriented guest atoms (2) play a crucial role in the emergence of glasslike thermal/dynamic properties in the THz-frequency region.

ACKNOWLEDGMENTS

This work is supported by the National Natural Science Foundation of China Grant No. 11334007. T.N. acknowledges support from the Grand-in-Aid for Scientific Research from the MEXT in Japan, Grant No. 26400381. J.Z. is supported by the program for Professor of Special Appointment (Eastern Scholar) at Shanghai Institutions of Higher Learning, Program No. TP2014012.

[1] G. A. Slack, in *CRC Handbook of Thermoelectrics*, edited by D. M. Rowe (CRC, Boca Raton, FL, 1995), pp. 407–440.
[2] M. Beekman, D. T. Morelli, and G. S. Nolas, Nat. Mater. **14**, 1182 (2015).
[3] See the review, for example, in T. Takabatake, K. Suekuni, T. Nakayama, and E. Kaneshita, Rev. Mod. Phys. **86**, 669 (2014), and references therein.
[4] B. C. Sales, B. C. Chakoumakos, R. Jin, J. R. Thompson, and D. Mandrus, Phys. Rev. B **63**, 245113 (2001).
[5] C. W. Myles, K. Biswa, and E. Nenghabi, Physica (Amsterdam) B **401-402**, 695 (2007).
[6] S. Pailhes, H. Euchner, V. M. Giordano, R. Debord, A. Assy, S. Gomes, A. Bosak, D. Machon, S. Paschen, and M. de Boissieu, Phys. Rev. Lett. **113**, 025506 (2014).
[7] T. Tadano, Y. Gohda, and S. Tsuneyuki, Phys. Rev. Lett. **114**, 095501 (2015).
[8] M. L. Williams and H. J. Maris, Phys. Rev. B **31**, 4508 (1985); K. Yakubo, T. Nakayama, and H. J. Maris, J. Phys. Soc. Jpn. **60**, 3249 (1991).
[9] See the review, for example, in T. Nakayama and K. Yakubo, Phys. Rep. **349**, 239 (2001).
[10] See Supplemental Material at http://link.aps.org/supplemental/10.1103/PhysRevB.93.214305 for the details of the FOM method and the convergence of calculations.
[11] S. Christensen, M. A. Avila, K. Suekuni, R. Pilt, T. Takabatakeb, and M. Christensen, Dalton Trans. **42**, 14766 (2013).
[12] M. A. Avila, K. Suekuni, K. Umeo, H. Fukuoka, S. Yamanaka, and T. Takabatake, Phys. Rev. B **74**, 125109 (2006); Appl. Phys. Lett. **92**, 041901 (2008); K. Suekuni, M. A. Avila, K. Umeo, H. Fukuoka, S. Yamanaka, T. Nakagawa, and T. Takabatake, Phys. Rev. B **77**, 235119 (2008).
[13] See Supplemental Material at http://link.aps.org/supplemental/10.1103/PhysRevB.93.214305 for the calculated results of $S(\boldsymbol{Q},E)$ in the direction [hh0] different from [h00] in Figs. 2 and 3 and the selection rules for the [h00] direction.
[14] C. H. Lee, H. Yoshizawa, M. A. Avila, I. Hase, K. Kikou, and T. Takabatake, J. Phys. Conf. Ser. **92**, 012169 (2007).
[15] M. Christensen, A. B. Abrahamsen, N. B. Christensen, F. Juranyi, N. H. Andersen, K. Lefmann, J. Andreasson, C. R. H. Bahl, and B. B. Iversen, Nat. Mater. **7**, 811 (2008).
[16] T. Mori, S. Goshima, K. Iwamoto, S. Kushibiki, H. Matsumoto, N. Toyota, K. Suekuni, M. A. Avila, T. Takabatake, T. Hasegawa, N. Ogita, and M. Udagawa, Phys. Rev. B **79**, 212301 (2009).
[17] Y. Takasu, T. Hasegawa, N. Ogita, M. Udagawa, M. A. Avila, K. Suekuni, I. Ishii, T. Suzuki, and T. Takabatake, Phys. Rev. B **74**, 174303 (2006); Y. Takasu, T. Hasegawa, N. Ogita, M. Udagawa, M. A. Avila, K. Suekuni, and T. Takabatake, *ibid.* **82**, 134302 (2010).

[18] M. Christensen, S. Johnsen, F. Juranyi, and B. B. Iversen, J. Appl. Phys. **105**, 073508 (2009).
[19] M. Nakamura and M. Arai (private communications).
[20] A. Yamakage and Y. Kuramoto, J. Phys. Soc. Jpn. **78**, 064602 (2009).
[21] T. Nakayama and E. Kaneshita, J. Phys. Soc. Jpn. **80**, 104604 (2011).
[22] K. Iwamoto, S. Kushibiki, H. Honda, S. Kajitani, T. Mori, H. Matsunoto, N. Toyota, K. Suekuni, M. A. Avila, and T. Takabatake, J. Phys. Soc. Jpn. **82**, 024601 (2013).
[23] T. Mori, K. Iwamoto, S. Kushibiki, H. Honda, H. Matsumoto, N. Toyota, M. A. Avila, K. Suekuni, and T. Takabatake, Phys. Rev. Lett. **106**, 015501 (2011).
[24] Y. Inamura, M. Arai, M. Nakamura, T. Otomo, N. Kitamura, S. M. Bennington, A. C. Hannon, and U. Buchenau, J. Non-Cryst. Solids **293-295**, 389 (2001).
[25] See the review, for example, in T. Nakayama, Rep. Prog. Phys. **65**, 1195 (2002).
[26] T. Nakayama and E. Kaneshita, Europhys. Lett. **84**, 66001 (2008).